Circular wire-bundle superscatterer

Sergei Kosulnikov [a,b,1,*], Dmytro Vovchuk [a,1], Roman E. Noskov [a], Andrey Machnev [a], Vitali Kozlov [a], Konstantin Grotov [b], Konstantin Ladutenko [b], Pavel Belov [b], Pavel Ginzburg [a]

[a] Tel Aviv University, Ramat Aviv, Tel Aviv 69978, Israel
[b] School of Physics and Engineering, ITMO University, Saint Petersburg 197101, Russia

ARTICLE INFO

ABSTRACT

Scattering cross-section is one of the main properties, characterizing an object in wireless applications. Resonant phenomena increase the electromagnetic visibility of a scatterer while keeping its footprint small. However, the single-channel limit or Chu-Harrington limit imposes a tight upper bound on a scattering cross-section of subwavelength objects. Being derived for a dipolar response, this limitation can be bypassed if several resonances of a structure are spectrally co-located and contribute constructively to the scattering. Subwavelength structures, obeying this design concept though hardly achievable in practical implementations, are called superscatterers. Here we demonstrate a superscatterer realization, based on a circular bundle of vertically aligned metal wires, optimized to demonstrate 5 multipoles, resonating at nearly the same frequency. As a result, the scattering cross-section becomes 12 times larger than object's geometrical cross-section. Owing to the multipolar multiplexing within the structure, the scattering is 7 times larger than the dipole single-channel limit. Additionally, as a result of the constructive interference of several multipoles, scattering directivity up to 10 dB is observed. Wire-bundle superscatterers may become an attractive architecture for many applications, including compact directive antennas, radar chaff and beacons, long-range RFID tags, and many others.

© 2022 Elsevier Ltd. All rights reserved.

1. Introduction

Tailored electromagnetic scattering governs a wide range of wireless communications, where efficient antennae and beacons are required to support reliable links. Typically, these devices are separated into two categories, each obeying different design rules. While electrically large structures can be addressed by physical optics tools, elements with wavelength-comparable features require full-wave analysis [1]. Here we consider small scatterers with an aim to increase their scattering cross-sections. This special property is especially valuable in a range of low frequency (typically below 10 GHz) applications, including miniature RFID tags [2–4], small radar beacons and radar chaff [5–9]. In the optical domain, highly scattering subwavelength plasmonic and all-dielectric particles are used in solar cells, thermal therapy, color displays, lithography, and many other nanophotonic applications [10–13].

Maximal scattering efficiency of a resonant object depends several parameters, though it does not depend on scatterer's size when low-loss materials are in use. The quality factor of the resonance, however, drops dramatically with the size reduction and

is bounded from below by the Chu-Harrington limit [14,15]. While the beforehand discussion is applied to objects operating on dipole resonances, the contribution of higher-order multipoles changes the picture quite dramatically. The contribution of a spherical resonant multipole (a channel) to the scattering cross-section is limited by $(2\ell+1)\lambda^2/(2\pi)$, where ℓ is a total angular momentum. Typically, a single-channel limit is defined for a dipole resonance, for which $\ell=1$ and, consequently, the maximal scattering cross-section is $3\lambda^2/(2\pi)$ [16]. Operation on higher-order multipoles, e.g. magnetic quadrupole or octupole, can, in principle, improve the scattering efficiency [17,18], constrained by symmetry group considerations. Furthermore, the spectral overlap of several resonances makes an additive contribution to the overall performance of a structure. Subwavelength objects, demonstrating scattering efficiently above the single channel limit, are called superscatterers. Several superscatterer designs have been proposed and include a core-shell multilayer sphere [18] and a multilayer cylinder [16,19]. At a microwave frequency range, the superscattering effect was experimentally shown for a multilayer cylinder, e.g. in [20]. It is worth noting that the beforehand mentioned structures have closed-form analytical solutions, which allow performing a fast optimization over a large set of parameters to design spectral overlap of several resonances. Typically, this task is quite involved, as eigenfrequencies of a system, based on strongly coupled resonators, can
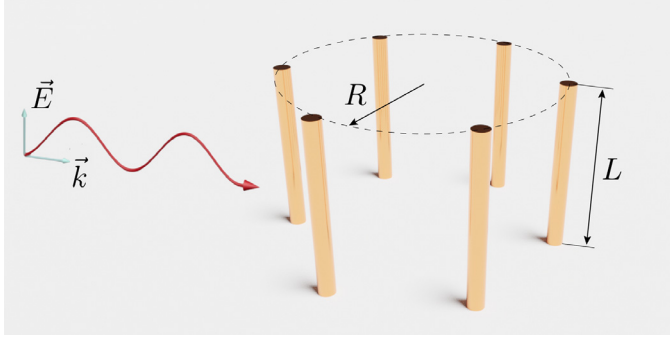
Fig. 1. Schematics of a circular wire bundle-a set of vertically aligned wires are equidistantly distributed on a cylinder surface.

differ significantly from those, obtained with a negligible coupling. To obtain a high level of modal degeneracy extensive efforts are required [21], including geometrical symmetry breaking approaches [22]. Taking into account those constrains, several complex structures were recently reported [23,24]. Scattering performances are typically assessed versus the dipole single-channel limit. For example, a subwavelength corrugated cylinder [24] was shown to bypass the limit by a factor of 3–6, while multilayered cylinders demonstrated an improvement by a factor of 4–6 [20,25].

While the beforehand mentioned designs of superscatterers were capable to surpass the limit, they all share the same fundamental constraint. Working with higher-order resonances necessarily implies having a strong near-field accumulation. This stored energy is dissipated due to material losses of constitutive elements. Consequently, lossy materials and lumped elements in superscatterers architectures possess the main constraints, limiting the performances.

Here we investigate a structure made of vertically aligned highly conductive (copper) wires, placed in a densely packed circular array-a bundle (Fig. 1). The wires are thrust in a foam host, which is transparent for GHz waves. We optimized the structure towards spectral overlap of resonances and succeeded in the co-location of five lower-order multipoles. As a result, the dipolar single-channel limit was overcome by a factor of 7. The structure was tested at an anechoic chamber, demonstrating the scattering cross-section of 80 cm^2, while its geometrical area is only $2RL = 6.6$ cm^2. Though the overall scattering cross-section is a superscatterer performance measure, the directivity also plays a role in many wireless applications. This factor is governed by relative phases between multipole contributions. Here, an additional outcome of our investigation is a strong forward scattering, approaching directivity of 10.5 dB at the operational region.

The manuscript is organized as follows: electromagnetic properties of a 6-wire bundle are investigated numerically and parameters for the high-scattering regime are identified. Detailed studies of the phenomenon are performed next and 'multipoles to eigenmodes mapping' is provided, revealing the main mechanism of the superscattering. Then an experimental confirmation of the obtained results is given before final discussions, concluding this work.

2. Wire bundle resonator: numerical analysis and optimization

2.1. Scattering analysis

Wire bundle resonator was taken as a test object owing to its overall parametrization simplicity with though a large number of independent degrees of freedom. The structure is characterized by several parameters, which can be considered as degrees of free-

dom in optimization. Here, the resonator radius will be taken as a variable and an additional frequency sweep will assist in finding characteristic spectral features. While it is quite clear that several resonant multipoles should be spectrally overlapped and interfere with proper amplitudes and phases, there is no recipe how to find out a suitable geometry. We have taken a geometry, based on 6 wires, which is an empirically obtained compromised number. This structure has 4 modes, which emerge from hybridization of dipolar resonances on individual wires, as it will be discussed in details hereinafter. Taking a larger number of wires makes the modal hierarchy much more complex, while taking fewer does not provide a state of the art performance, as we found empirically. Dimensions of each individual wire were fixed – 20 mm in length and 1 mm in diameter. The finite diameter of the wire introduces a correction to its dipolar resonance, shifting it to a lower frequency - $f_0 \approx 6.45$ GHz in this case. Wire's material is copper with its moderately low ohmic losses (electric conductivity is $5.96 \cdot 10^7$ S/m). A dense package of the wires in the bundle gives rise to a significant near-field coupling. The latter leads to modes hybridization, which tremendously changes the electromagnetic properties of the structure. In order to investigate this effect, we performed a numerical analysis of scattering using CST Microwave studio, frequency domain solver. Fig. 2(a) is a color map, demonstrating the scattering cross-section normalized to the single-channel dipole limit ($\sigma_{tot} = 3\lambda^2/(2\pi)$), as a function of the resonator radius R and the operation frequency f. Scattering boundary conditions have been applied on the calculation domain, which was taken to be twice larger than the scatterer. The incident field is linearly polarized along the wires (Fig. 1). The color map allows identifying three resonant branches, which start overlapping at a certain frequency range if the structure radius is properly chosen.

To understand the predicted highly efficient scattering phenomenon, a detailed analysis will be performed next. To bypass the single-channel limit, several resonant multipoles should interfere constructively with a proper relative phase to build up a strong scattered field. However, multipoles are not eigenmodes of the structure and the system response is built up by its resonant modes. While a trivial mapping between resonances and multipoles does exist for structures with rotational symmetry, in the general case each eigenmode can have far-field radiation, composed of several multipolar contributions. For example, Mie modes in isotropic cylinders and spheres, being exited by an incident wave, have far-field signatures in a form of spherical multipoles [14]. Eigen modes in structures with broken or incomplete (even discrete rotational symmetry) symmetries require several spherical multipoles for describing far-field scattering. Circles in Fig. 2(a,b) demonstrate radius-dependent dispersion of the eigenmodes. Those modes in this system can be described with phase of surface currents, flowing on the wires. E.g. fundamental dipolar mode, where there is no any change in the phase over the wires in the system is defined as *m0*, mode with 1 phase variation is *m1*, etc. Relevant modes are depicted in the right inset to Fig. 2. Lines in Fig. 2(d,e) show the dispersion of the multipoles [26]. In the multipole decomposition we consider electric dipole (ED), magnetic dipole (MD), electric and magnetic quadrupoles (EQ and MQ), and electric and magnetic octupoles (EO and M0) [27–29]. Obviously, those resonant branches do overlap, but there is no one-to-one mapping between them. This behavior will be further discussed in detail.

2.2. Eigenmode analysis

The total number of modes in a bundle (or circular wire array) consisting of N wires equals $(N + 1)/2$ if N is odd or $N/2 + 1$ if N is even [30–32]. Hybridization between higher-order modes of individual wires is neglected, as it leads to resonances at much
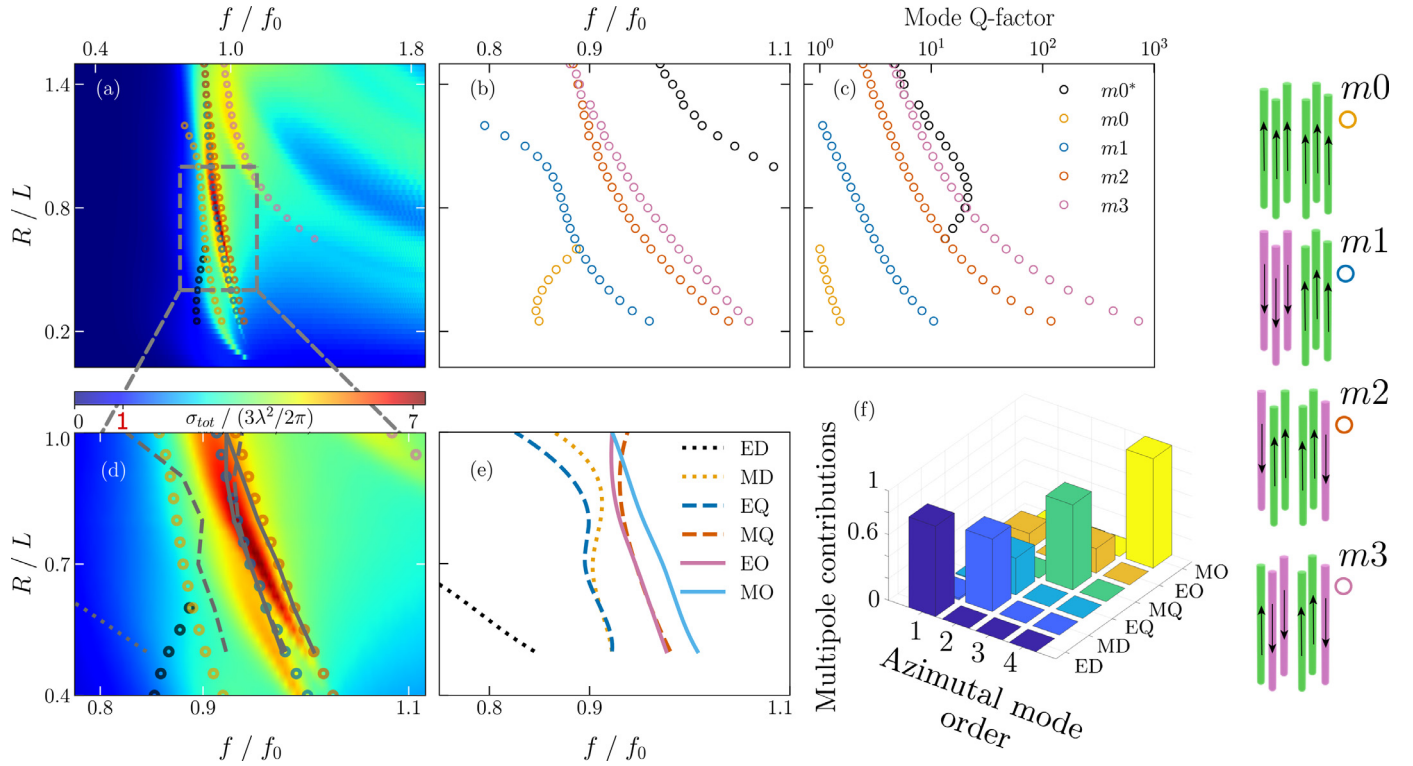
Fig. 2. Numerical analysis of a wire-bundle scatterer. (a) Scattering cross-section, normalized to a theoretical single-channel limit (dipole limit $3\lambda^2/(2\pi)$), as a function of bundle's radius and operational frequency. Circles show the corresponding resonant eigenmodes. (b) Eigenmodes dispersion, as a function of radius, see legend to the next panel. (c) Quality factors of the eigenmodes as a function of radius. (d) 'Zoom in' on panel (a), the focus is on the main area of interest, where the scattering cross-section is maximal. Circles indicate eigenmodes from panel (b), lines indicate the multipolar resonant branches from panel (e). (e) Multipoles dispersion, as a function of radius. Colored lines correspond to multipoles with abbreviations, explained in the main text. (f) Eigenmodes to multipoles mapping. The histogram is the weighted (normalized) multipole expansion of each eigenmode's far-field pattern. (*m0-m3*) Four non-degenerate eigenmodes of the structure, shown as phases of currents on the wires, $R = 5$ mm.

higher frequencies. Six-wire system supports four nondegenerate modes *m0-m3*, if only dipole resonances on the wires are considered. The modes can be classified with an azimuthal number, since phase variations of currents on the wires obey the geometrical periodicity of the structure according to the Bloch theorem. It is worth noting, however, that *the azimuthal number* has no direct relation to spherical harmonics (Y_l^m), as it will be shown hereinafter.

The analysis was performed with CST, eigenmode solver, capable to address open resonators and estimate quality factors (Q-factors) of the modes. Fig. 2(b) shows the eigenmode dispersion as a function of the structure radius. Fig. 2(*m0-m3*) shows the phases of the currents on the wires. For example, *m0* is the fundamental mode with 6-fold rotational symmetry. Higher-order modes have alternating phases of the currents, and the index here shows the number of zero crossings times two. At higher frequencies another dipolar-like mode *m0** emerges and it results from hybridization of higher-order contributions of the finite-length wires. *m0** has a relatively high Q-factor and affects the scattering at higher frequencies without a significant impact on the region of our interest. Next, it is worth noting that not all the modes contribute equally to the scattering. Their influence can be assessed by calculating the Q-factors, presented in Fig. 2(c). Q-factor is formed by an interplay between radiation and material losses. In the case of highly conductive low loss materials, radiation losses predominate – this can be seen by comparing *m1* (predominantly electrical dipole mode, high radiation efficiency) and *m3* (predominantly magnetic octupole mode, high near-field concentration). This justification can be made by observing Fig. 2(f), which will be discussed in detail hereinafter. Fig. 2(c) shows that *m2* and *m3* are the main contributors to the scattering owing to the finite dimension of the structure.

In order to reveal the eigenmode contribution to the scattering efficiency, the far-field should be expanded by a series of multipoles, which will be done next.

2.3. Multipole expansion

To assess the scattering performance versus the single-channel limit, the multipole expansion was performed. Here we use a spherical multipole basis [27] with six multipoles, which are appropriate to demonstrate convergence to the total scattering with a sufficient accuracy. Multipole dispersion as a function of the bundle's radius appears in Fig. 2(e). It is quite remarkable that five multipoles are almost perfectly co-located at the region, where the scattering cross-section is maximized ($R = 16$ mm, $f = 6.025$ GHz). This overlap is made possible due to the finite Q-factors. Note, that the multipoles from the same symmetry group repel each other. Here, this repulsion is smaller than full width at half maximum of individual peaks.

2.4. Eigenmodes-multipoles mapping

Finally, the relation between the eigenmodes and multipoles can be made. This is done by expanding the far-field of an eigenmode using spherical harmonics. The task was performed numerically. The results are summarized in the histogram – Fig. 2(f). It can be seen that the fundamental eigenmode *m0* is primarily ED with a small contribution of EO. The latter is the result of retardation, originating from a finite size of the structure. Higher-order *m3* mode is solely MO. Eigenmodes *m1* and *m2* are the mixtures of four multipoles – EQ, EO, MD, and MQ. Now, the result is evident – two resonant eigenmodes contribute to scattering, which is

formed by four resonant multipoles. The fifth multipole (MO) resonates nearly at the same frequency, but does not contribute to the scattering. It is linked to eigenmode *m3*, which is not excited by the incident plane wave.

2.5. Far-field scattering patterns

Since higher-order multipoles have nontrivial far-field signatures, their interference can result in peculiar patterns. In this case, another possible and important outcome of the investigation is the capability to obtain a directive scattering. From the theoretical standpoint, so-called 'Einstein needle-like radiation' can be obtained if all multipoles constructively interfere with weighted amplitudes and adjusted relative phases (e.g. seminal Oseen's report [33]). However, there are numerous practical constraints, related to fabrication tolerance and internal material losses (e.g. [34]).

Electrically small antennas/scatterers, satisfying the condition $kr < 1$ (k is a free space wavenumber and r is the smallest radius of a sphere, enclosing the structure) have inherently small bandwidth and directivity, bounded from above by well-known Chu-Harrington [35,36] and Geyi [37] limits. An executive summary was done by Pigeon et al. [38]. Those limits, as a function of normalized structure's size, are plotted in Fig. 3(a). Harrington's directivity limit is $D_{max} = \iota^2 + 2\iota$ (where $\iota = kr$) can be taken as an estimate, having a simple closed-form expression. Both Chu-Harrington and Geyi limits predict a significant drop in the gain with the structure's size reduction. Overcoming those limits remains a very challenging and rewarding task, as was mentioned in the Introduction. To assess the performance of our structure, we put a point on the graph, corresponding to $R = 16$ mm structure. It can be clearly seen that both limits were overcome by several dBs. This is the result of a partial interference of four multipoles, while Chu-Harrington predicts having only two, according to the formula above.

Whereas in [38] authors provided an executive summary on subwavelength scatterer performances, it is worth noting other approaches, based on machine learning optimization techniques. For example, highly directive antennas and scatterers were reported (e.g. [39] and [40]), nevertheless they do fall into 'electrically small' category.

The directivity of our structure as the function of its parameters appears in Fig. 3(b). High directivity can be obtained for a broad range of parameters. However, this measure is less practical, as high directivity should be accompanied by a high scattering for an efficient interaction. Those two properties, being obtained together, have practical implications. Fig. 3(c) is the product of the directivity (linear scale) and the scattering cross-section. This figure of merit has a clear maximum, where the device has a strong directive forward scattering, making it operating as a high-performance Huygens element.

3. Experimental demonstration

As it was mentioned in the Introduction, our architecture has a very high fabrication tolerance and does not include any lossy materials. We use copper, which is almost lossless material at the considered frequency range (skin depth $\delta < 1.5$ μm at the considered frequency range).

Our experimental demonstration is performed on five different samples, which appear in the inset to Fig. 4(a). Scattering experiments were performed at an anechoic chamber. Two broadband horn antennas NATO IDPH-2018 (Tx and Rx), placed 2 m apart, were used to transmit and receive the signals. The samples were located in the middle. Complex S-parameters (S_{12} and S_{11} -
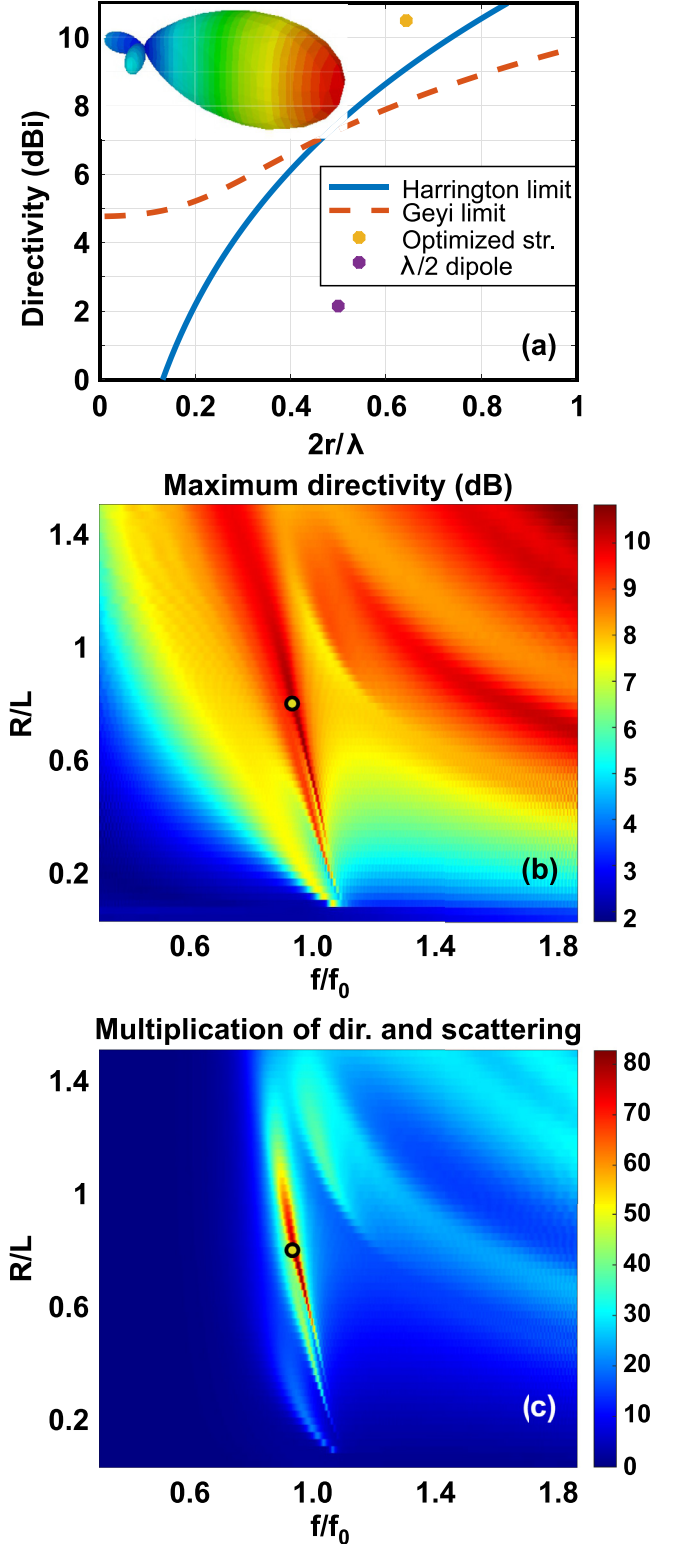

Fig. 3. (a) Chu-Harrington and Geyi directivity bounds as a function of structure size, normalized to the wavelength. Purple point-half-wavelength dipole. Yellow point - our structure ($R = 16$ mm), overcoming both limits. (b) Directivity's of a 6-wire bundle (dB scale) as a function of normalized radius (to the wire's length, $L = 20$ mm) and the normalized frequency (1 corresponds to the directivity maximum). (c) Product of directivity (linear scale) and the scattering cross-section normalized to single-channel, presented in Fig. 2(a).
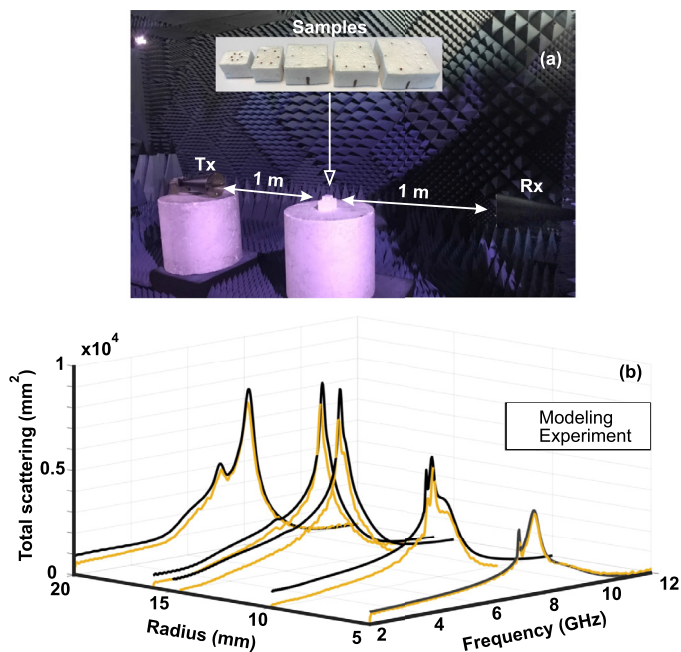
Fig. 4. (a) Experimental setup-anechoic chamber, two horn antennas (Tx and Rx), and a styrofoam stage for samples. Inset-photographs of five samples under test. (b) Total scattering versus radius of structure and frequency for five different samples -experiment and modeling.

transmission and reflection) were acquired with Microwave Network Analyzer Keysight N5232b. Data acquisition was done in the range between 2 and 12 GHz. The total scattering cross-sections of the object in mm^2 was extracted by applying the optical theorem. 100 mm diameter brass disk was used as a calibration tool. Forward and inverse Fourier transformations were applied to perform the time-domain filtering.

The experimental samples were made from foam holders and copper wires – 20 mm length, 1 mm diameter. Those parameters were used in the numerical analysis in all the previous sections. The radii of the bundles are as follows - $R = 5$ and 10 mm (before the resonances overlap), $R = 15$ and 16 mm (where the perfect interference takes place), and $R = 20$ mm (where the resonant condition breaks down). Fig. 4 summarizes the experimental results. Fig. 4(a) demonstrates the overall experimental set-up and surrounding environment of the anechoic chamber. Fig. 4(b) provides the detailed quantitative comparison between scattering cross sections of the considered samples and numerical predictions. It is quite remarkable that the numerical data fit perfectly the experiment. There are two main reasons for that – the choice of the structure (its simplicity) and an accurate calibration of the experimental setup. In terms of achievable parameters, the obtained scattering cross-section is as high as 8000 mm^2, which prevails the single-channel limit by a factor of 7.

4. Outlook and conclusion

The wire-bundle resonator has been designed to demonstrate superscattering performances, which were subsequently experimentally demonstrated. The core of the effect is the spectral overlap between several resonances of the structure. However, simultaneous excitation of several eigen modes within a structure does not guarantee a high scattering. Spherical multipoles, forming a complete orthogonal basis to span the far-field, provide a complete information on scattering. However, mapping between eigenmodes and resonant multipoles is not trivial for structures lacking a continuous rotational symmetry. As a result, each eigen-

mode, leaking to the far-field, can excite several multipoles and, consequently, contribute to many scattering channels. Our structure was shown to operate on two resonant modes and, which is critical, on four resonant multipoles, granting it superscattering performances. Furthermore, constructive interference between several multipoles leads to super-directive scattering, which overcomes Chu-Harrington and Geyi limits. While Cho-Harrington theory predicts having two resonant multipoles in the structure, our design demonstrates four, elevating the directivity above the commonly accepted limitation. Further increasing the number of wires in the bundle and, probably, breaking its internal symmetry can lead to elevated performances both in scattering and directivity. These concepts might open new venues in many wireless applications, including radar deception, point-to-point communications at lower frequencies, and many others. For example, constructing low-frequency compact directive antennas with a bandwidth, sufficient for wireless communications, remains a challenge.

Declaration of Competing Interest

The authors declare that they have no known competing financial interests or personal relationships that could have appeared to influence the work reported in this paper.

CRediT authorship contribution statement

Sergei Kosulnikov: Conceptualization, Methodology, Validation, Formal analysis, Investigation, Writing – original draft. **Dmytro Vovchuk:** Methodology, Validation, Visualization, Writing – original draft. **Roman E. Noskov:** Conceptualization, Validation, Visualization. **Andrey Machnev:** Software, Validation, Data curation. **Vitali Kozlov:** Validation, Data curation, Visualization. **Konstantin Grotov:** Validation, Data curation, Visualization. **Konstantin Ladutenko:** Methodology, Formal analysis, Writing – original draft. **Pavel Belov:** Conceptualization, Methodology, Supervision. **Pavel Ginzburg:** Conceptualization, Methodology, Supervision, Project administration, Writing – review & editing, Funding acquisition.

Acknowledgments

References

[1] Balanis CA. Antenna theory analysis and design. 3rd ed. Hoboken: Wiley; 2005.
[2] Cui L, Zhang Z, Gao N, Meng Z, Li Z. Radio frequency identification and sensing techniques and their applications-a review of the state-of-the-art. Sensors 2019;19(18):4012. doi:10.3390/s19184012.
[3] Chen SL. A miniature RFID tag antenna design for metallic objects application. IEEE Antennas Wirel Propag Lett 2009;8:1043–5. doi:10.1109/LAWP.2009.2032252.
[4] Dobrykh D, et al. Long-range miniaturized ceramic RFID tags. IEEE Trans Antennas Propag 2020. doi:10.1109/TAP.2020.3037663.
[5] Levanon N, Mozeson E. Radar signals. Hoboken, NJ, USA: John Wiley & Sons, Inc; 2004.
[6] Filonov D, Shmidt A, Boag A, Ginzburg P. Artificial localized magnon resonances in subwavelength meta-particles. Appl Phys Lett 2018;113(12):123505. doi:10.1063/1.5047445.
[7] Dobrykh D, et al. Multipole engineering for enhanced backscattering modulation. Phys Rev B 2020;102(19):195129. doi:10.1103/PhysRevB.102.195129.
[8] Dobrykh D, Mikhailovskaya A, Ginzburg P, Filonov D. 4D optically reconfigurable volumetric metamaterials. Phys Status Solidi Rapid Res Lett 2020;14(8):2000159. doi:10.1002/pssr.202000159.
[9] Komissarov R, Kozlov V, Filonov D, Ginzburg P. Partially coherent radar unties range resolution from bandwidth limitations. Nat Commun 2019;10(1423):1–9. doi:10.1038/s41467-019-09380-x.

[10] Maier SA. Plasmonics: fundamentals and applications. New York: Springer Science & Business Media; 2007.

[11] Berkovitch N, Ginzburg P, Orenstein M. Nano-plasmonic antennas in the near infrared regime. J Phys CondensMatter 2012;24(7):073202.

[12] Kuznetsov AI, Miroshnichenko AE, Brongersma ML, Kivshar YS, Luk'yanchuk B. Optically resonant dielectric nanostructures. Science 2016;354(6314):aag2472. doi:10.1126/science.aag2472.

[13] Noskov RE, et al. Golden vaterite as a mesoscopic metamaterial for biophotonic applications. Adv Mater 2021;33(25):2008484. doi:10.1002/adma.202008484.

[14] Harrington RF. Time-harmonic electromagnetic fields. 2nd ed. New York: Wiley-IEEE Press; 2001.

[15] Kosulnikov S, Filonov D, Boag A, Ginzburg P. Volumetric metamaterials versus impedance surfaces in scattering applications. Sci Rep 2021;11(1):9571. doi:10.1038/s41598-021-88421-2.

[16] Ruan Z, Fan S. Superscattering of light from subwavelength nanostructures. Phys Rev Lett 2010;105(1):013901. doi:10.1103/PhysRevLett.105.013901.

[17] Tribelsky MI, Luk'yanchuk BS. Anomalous light scattering by small particles. Phys Rev Lett 2006;97(26):263902. doi:10.1103/PhysRevLett.97.263902.

[18] Ruan Z, Fan S. Design of subwavelength superscattering nanospheres. Appl Phys Lett 2011;98(4):043101. doi:10.1063/1.3536475.

[19] Mirzaei A, Shadrivov IV, Miroshnichenko AE, Kivshar YS. Cloaking and enhanced scattering of core-shell plasmonic nanowires. Opt Express 2013;21(9):10454. doi:10.1364/OE.21.010454.

[20] Qian C, et al. Experimental observation of superscattering. Phys Rev Lett 2019;122(6):063901. doi:10.1103/PhysRevLett.122.063901.

[21] Ginzburg P, Berkovitch N, Nevet A, Shor I, Orenstein M. Resonances on-demand for plasmonic nano-particles. Nano Lett 2011;11(6):2329–33.

[22] Krasikov S, et al. Multipolar engineering of subwavelength dielectric particles for scattering enhancement. Phys Rev Appl 2021;15(2):024052. doi:10.1103/PhysRevApplied.15.024052.

[23] Lee T, Nomura T, Schmalenberg P, Dede EM, Iizuka H. Directional acoustic superscattering by coupled resonators. Phys Rev Appl 2019;12(5):054059. doi:10.1103/PhysRevApplied.12.054059.

[24] Shcherbinin VI, Fesenko VI, Tkachova TI, Tuz VR. Superscattering from subwavelength corrugated cylinders. Phys Rev Appl 2020;13(2):024081. doi:10.1103/PhysRevApplied.13.024081.

[25] Qian C, et al. Multifrequency superscattering from subwavelength hyperbolic structures. ACS Photonics 2018;5(4):1506–11. doi:10.1021/acsphotonics.7b01534.

[26] Bohren CF, Huffman DR. Absorption and scattering of light by small particles. New York: Wiley; 1998.

[27] Jackson JD. Classical electrodynamics. 3rd ed. John Wiley & Sons; 1998.

[28] Alaee R, Rockstuhl C, Fernandez-Corbaton I. An electromagnetic multipole expansion beyond the long-wavelength approximation. Opt Commun 2018;407:17–21. doi:10.1016/j.optcom.2017.08.064.

[29] Terekhov PD, Evlyukhin AB, Redka D, Volkov VS, Shalin AS, Karabchevsky A. Magnetic octupole response of dielectric quadrumers. Laser Photon Rev 2020;14(4):1900331. doi:10.1002/lpor.201900331.

[30] Collin RE, Zucker FJ. Antenna theory. McGraw-Hill; 1969. no. ч. 7,№ 1.

[31] Josefsson L, Persson P. Conformal array antenna theory and design. Hoboken, New Jersey: John Wiley & Sons, Inc; 2006.

[32] King RWP, Fikioris GJ, Mack RB. Cylindrical antennas and arrays. Cambridge; 2002.

[33] Oseen CW. Die einsteinsche nadelstichstrahlung und die maxwellschen gleichungen. Ann Phys 1922;374(19):202–4. doi:10.1002/andp.19223741903.

[34] Hansen RCJohn Wiley & Sons . Electrically small, superdirective, and superconducting antennas. Wiley-Interscience; 2006.

[35] Chu LJ. Physical limitations of omni-directional antennas. J Appl Phys 1948;19(12):1163–75. doi:10.1063/1.1715038.

[36] Harrington R. On the gain and beamwidth of directional antennas. IRE Trans Antennas Propag 1958;6(3):219–25. doi:10.1109/TAP.1958.1144605.

[37] Geyi W. Physical limitations of antenna. IEEE Trans Antennas Propag 2003;51(8):2116–23. doi:10.1109/TAP.2003.814754.

[38] Pigeon M, Delaveaud C, Rudant L, Belmkaddem K. Miniature directive antennas. Int J Microw Wirel Technol 2014;6(1):45–50. doi:10.1017/S1759078713001098.

[39] Konstantinidis K, Feresidis AP, Hall PS. Broadband sub-wavelength profile high-gain antennas based on multi-layer metasurfaces. IEEE Trans Antennas Propag 2015;63(1):423–7. doi:10.1109/TAP.2014.2365825.

[40] Zucchi M, Giordanengo G, Righero M, Vecchi G. First demonstration of machine-designed ultra-flat, low-cost directive antenna. Sci Rep 2020;10(1):10506. doi:10.1038/s41598-020-67354-2.